Strengthening of Wood-like Materials via Densification and Nanoparticle Intercalation

David Novel [1,2], **Simone Ghio** [1,2], **Andrea Gaiardo** [2,3], **Antonino Picciotto** [2], **Vincenzo Guidi** [3], **Giorgio Speranza** [2,4,5], **Maurizio Boscardin** [2], **Pierluigi Bellutti** [2] and **Nicola M. Pugno** [1,6,7,*]

[1] Laboratory of Bio-Inspired, Bionic, Nano, Meta Materials & Mechanics, Department of Civil, Environmental and Mechanical Engineering, University of Trento, via Mesiano 77, I-38123 Trento, Italy; novel@fbk.eu (D.N.); simoneghio1@gmail.com (S.G.)

[2] Centre for Materials and Microsystems, Fondazione Bruno Kessler, via Sommarive 18, I-38123 Trento, Italy; gaiardo@fbk.eu (A.G.); picciotto@fbk.eu (A.P.); speranza@fbk.eu (G.S.); boscardi@fbk.eu (M.B.); bellutti@fbk.eu (P.B.)

[3] Department of Physics and Earth Science, University of Ferrara, via Saragat 1/c, I-44122 Ferrara, Italy; guidi@fe.infn.it

[4] Istituto di Fotonica e Nanotecnologie & Consiglio Nazionale delle Ricerche IFN—CNR, via alla Cascata 56/C Povo, I-38123 Trento, Italy

[5] Department of Industrial Engineering, University of Trento, via Sommarive 9, I-38123 Trento, Italy

[6] School of Engineering and Materials Science, Queen Mary University of London, Mile End Road, London E1 4NS, UK

[7] Ket Labs, Edoardo Amaldi Foundation, via del Politecnico snc, I-00133 Rome, Italy

* Correspondence: nicola.pugno@unitn.it

check for updates

Abstract: Recently, several chemical and physical treatments were developed to improve different properties of wood. Such treatments are applicable to many types of cellulose-based materials. Densification leads the group in terms of mechanical results and comprises a chemical treatment followed by a thermo-compression stage. First, chemicals selectively etch the matrix of lignin and hemicellulose. Then, thermo-compression increases the packing density of cellulose microfibrils boosting mechanical performance. In this paper, in comparison with the state-of-the-art for wood treatments we introduce an additional nano-reinforcemeent on densified giant reed to further improve the mechanical performance. The modified nanocomposite materials are stiffer, stronger, tougher and show higher fire resistance. After the addition of nanoparticles, no relevant structural modification is induced as they are located in the gaps between cellulose microfibrils. Their peculiar positioning could increase the interfacial adhesion energy and improve the stress transfer between cellulose microfibrils. The presented process stands as a viable solution to introduce nanoparticles as new functionalities into cellulose-based natural materials.

Keywords: cellulose-based nanocomposites; nanoparticles; densification; alkaline treatment; giant reed; structural modifications of natural materials

1. Introduction

Nowadays, research on natural materials and their technological optimization play a fundamental role in sustainable socio-economic development [1,2]. In particular, cellulose-based materials such as wood, bamboo, reed, and natural fibers have attracted enormous attention [3–7], given their high versatility suitable for a variety of applications including renewable energy source, fuel, comfort, furniture, construction, and recyclable packaging [4,8–10]. Moreover, chemically treated wood can be

turned into a transparent and conductive substrate for solar cells applications, flexible transistors, and electronics display such as liquid-crystal display (LCD) and organic light-emitting diode (OLED) [11,12]. In addition to the aforementioned applications, the most extensive utilization of timber since ancient times has been as a construction material, and it is still nowadays preferred over more modern building materials in a lot of instances due to a better life-cycle assessment, greater energy efficiency, lower costs, and near-to-zero waste by-product [13].

Wood, bamboo, and reed represent valid alternatives to steel and concrete not exclusively for socio-economic reasons but also for their structural qualities [7,14–17]. Through a combination of high strength and lightness, wood-like materials are strong competitors to modern construction materials [13]. Natural hollow materials, such as bamboo and reed, have superior tensile and flexural strength than wood [7,16,17]. Regarding these distinctive features, the exploitation of the intrinsically superior strength of hollow materials in the creation of larger and complex artefacts can generate a new strong competitor in the roster of construction materials. Nonetheless, the bare mechanical properties of bamboo are superior to those of giant reed and reed is considered to be a highly invasive and unwanted species [16,18–20].

The first historical records of the use of giant reed (arundo donax) dates back to Ancient Greece [21]. Nowadays, limited applications use reed, i.e., biofuel [22], industrial cellulose source [21], reed wattle for structural purposes, biomimetic, and technical textiles applications [6]. Due to its high biomass productivity [22], it can be exploited as a sustainable fast-growing and low-cost material [21].

The strength of arundo donax relies on its structural composition comprising cellulose fibers and hemicellulose embedded in a lignin matrix [19]. The cross-section analysis of reed culm showed a structure with a homogeneous density of fibers, which is increased in the cortical region being more rigid [19], showing mechanical properties superior of most type of woods [17]. Giant reed has developed, similarly to bamboo [5], an optimal stem structure, which is reinforced with internodes to overcome the weakness due to its hollow and slender conformation (i.e., Euler buckling) [20]. In fact, the internodes allow the giant reed to withstand high compressive and flexural loads, which would be impossible without their presence.

This work focuses on a novel chemical and structural modification to turn giant reed into an advanced material with extremely improved mechanical properties and higher stability under challenging environmental conditions. Giant reed specimens were treated in an alkaline environment to decrease the concentration of lignin and enable densification [23,24]. The removal of lignin and thermo-compression allowed to achieve a denser material with high structural performance [24]. Porosities occur because of the delignification process. We propose to exploit even these tiny spaces, filling them up with nanoparticles to make the material tougher.

Notwithstanding, several authors investigated the effect of inorganic nanostructured materials on wood or bamboo [25–28]. In this work we propose to tailor the effects of densification by introducing selected nanostructured materials in the structure of giant reed, i.e., silicon carbide (SiC) and graphene oxide (GO). On the one hand, SiC is a well-known material for its unique mechanical strength, which was exploited to improve the mechanical properties of metals [29], polymers composites [30], and cellulose-based materials [31]. On the other hand, GO flakes were chosen for its 2D structure with high aspect ratio exposing a high concentration of hydrogen bonds [32] to the cellulose/lignin units present in the reed as GO flakes proved to effectively enhance mechanical performance in cellulose-based materials [33]. The final yield of this process can further improve the strength and toughness compared to the same densified reed. The analyses carried out highlighted a significant increase in the mechanical properties of densified samples intercalated with nanoparticles, especially regarding stiffness, strength, and toughness. The addition of nanoparticles in the densified reed resulted also in a reduced water uptake by the reed, which decreases its biodeterioration [16,34] and thus guarantees a longer lifespan. Furthermore, the densified and nanoparticles intercalation treatments strongly increased the fire-retarding properties of the native reed and the "thermo-indentation" resistance, measured by using a custom-developed technique.

2. Materials and Methods

Three years old giant reed, i.e., arundo donax, was used for this study. A mixture of sodium hydroxide (Sigma-Aldrich), sodium sulfite (>98%, Sigma-Aldrich, St. Louis, MO, USA), and deionized (DI) water was used for the partial removal of lignin from the reed. After the lignin etching, reed specimens were immersed in silicon carbide (3C–SiC, purity >99%, Tec Star, Castelfranco Emilia, Italy) or graphene oxide (GO, water dispersion 4 mg/mL, monolayer content >95%, Graphenea, San Sebastian, Spain). A Bench Press (Pneumtic Table Top Press 2.5 Tons by Gibitre Instruments, Bergamo, Italy) was used to thermo-compress samples.

All the specimens were extracted from the culm of giant reed. Their orientation was parallel to sclerenchyma fibers, and they were mechanically polished to a regular geometry ($10 \times 2 \times 0.5$ cm^3). The cross-section of samples is perpendicular to the fibers' direction, while the lateral side is parallel to them. Then, the specimens were immersed in a re-fluxed boiling water solution containing NaOH (2.5 M) and Na$_2$SO$_3$ (0.4 M) to partially remove lignin.

The initial concentration of lignin for the arundo donax samples can be inferred from literature, when the age of the giant grass is known. In our case, the starting content of Lignin is about 22% [35]. The exposition time in alkaline solution was chosen according to the results achieved by Song et al., which showed that a decrease of about 50% in lignin content delivers the best mechanical properties [24], we conclude that the final concentration of lignin in our experiment is about 11%. Chemicals were removed from etched specimens by thoroughly washing samples in several boiling baths of deionized water, followed by washings with running deionized water. Chemically etched samples after delignification were dried overnight at 30 °C.

Afterwards, three sets of samples were prepared and each of them was subjected to a different treatment. The first reference set (labelled: D) was immersed in water, the second (D + SiC) was intercalated with SiC nanoparticles, and the third (D + GO) with GO (graphene oxide) flakes. To this aim, giant reed specimens were immersed in SiC and GO aqueous solutions (both at a concentration of 1 mg/mL). Then, vacuum was applied to remove trapped air inside samples and the solutions were vigorously stirred for 24 h at room temperature. An autoclave treatment of 3 h at 5 bar pressure followed. Last, while being still wet, each set was hot-pressed at 100 °C and 5 MPa of pressure for 3 h. Properties of these samples are compared with two other sets: Natural reed (labelled R) and natural reed subjected only to thermo-compression (TC) at 100 °C under 5 MPa pressure for 3 h, an intermediate treatment useful as a comparison as it is already implemented in the industry [7].

Mechanical properties were measured with a displacement controlled, electromechanical testing machine from Messphysik Materials Testing (MIDI 10). Tensile testing was carried out five times for each of the five sets of samples. The speed of each test was computed to get the same strain rate in both the tensile tests and the lower fibers of samples under flexural loading. The Young's elastic modulus was calculated for all samples in the same deformation range, from 0.025% to 0.075%, which displays a linear elastic region for all samples. Stress-strain curves are reported until fracture.

Flexural tests were carried out with a three-point bending setup. Flexural tests were carried out three times for each of the five sets of samples. The span length between the two support cylinders was 19.2 mm, this distance was increased to 50 mm for natural bamboo to fulfill the geometry requirements of the ASTM Standard D790-17. The cross-head speed was computed to obtain a suggested 0.01 mm/mm/min of strain rate on the outer fiber of the flexural samples. Flexural stress-strain curves are reported until the maximum load.

Microstructural studies were performed with a field emission scanning electron microscope (JSM-7401F, JEOL Ltd., Tokyo, Japan) and profilometer technique. A stylus profilometer (P6, KLA Corporation, Milpitas, CA, USA) was used to analyze the cross-section of the five sets of samples and to reconstruct their 3D surface by merging line scans having a distance of 2 μm.

Roughness was calculated with root mean square (RMS) on a wide area. The morphology and chemical composition of specimens were analyzed by SEM and energy dispersive X-ray spectroscopy (EDX spectroscopy) techniques, by means of a SEM.

Burning tests were performed using a modified Taghiyari method [28] and a thermographic camera. The classical Taghiyari method has been modified to better fit the thermographic inspection of the process, and a Bunsen type burner was used to generate the free flame. The wood samples were placed perpendicularly to the floor, at 90° with respect to the flame direction, with the width facing the camera and the thickness directly above the flame. The normalized burned volume was computed as follows:

$$V_\rho(t) = \frac{A \cdot d(t)}{\rho} \tag{1}$$

where $V_\rho(t)$ is the normalized burned volume, A and ρ are the cross-section and density of the sample, and *d(t)* is the flame advancement and was computed considering the area having a sample temperature higher than 360 °C. In order to be able to cross compare the calorific value of samples with different microstructure, the burned volume was normalized by the density since the calorific value is related to sample mass, hence to the density if a constant volume is considered.

Thermo-indentation tests were performed using a hot conical tip indenter (17.7° apex angle) at 400 °C. The indenter was placed perpendicular to the lateral surface of the surface with an indentation force of 0.65 N for 5, 10, and 15 s. The burned area was calculated from the images of samples' surfaces.

Accelerated humidity absorption tests were performed in a climatic chamber with controlled humidity 97 ± 1% rH. The values of humidity absorption are reported in a mass increase from the dried state. At every sampling time five samples—one per set—were extracted from the chamber, transferred in a closed vial, and weighed.

The chemical composition of the virgin and treated samples was examined also by X-ray photoelectron spectroscopy (XPS) (Axis DLD Ultra, Kratos Analytical Ltd., Manchester, UK). The analysis consists of the acquisition of a wide spectrum at a pass energy of 160 eV to detect all the chemical elements constituent of the sample surface. Then, core lines of interest were acquired at a higher energy resolution using a pass energy of 20 eV. Since samples are nonconductive, charge compensation was needed. Optimal conditions of compensation were obtained minimizing the full width at half maximum of the core line peaks and maximizing their intensity. This leads to an energy resolution of ~0.3 eV. Finally, data reduction was performed using a software made in-house based on the R platform (https://www.r-project.org). For each core line, a linear background subtraction and Gaussian components were used for peak fitting.

3. Results and Discussion

Sample morphologies were analyzed by SEM and scanning profilometry to reveal the effects induced in the internal structure of giant reed by the treatments applied. To this aim, specimens were embedded in epoxy resin and polished to obtain a macroscopically flat surface for both the cross-section and the lateral side. The profilometry analysis on the lateral face (Figure 1) is very useful to evaluate the packing density of the internal parenchyma structure. These structures tend to collapse under the effect of the external pressure. The collapse is partial for thermo-compressed (TC) reed (Figure 1b) and it leads to a reduction in the lateral size of the cellular structure ranging from 65 to 46 μm. Conversely, densified (D) giant reed (Figure 1c) show an almost complete collapse in parenchyma cells and their lateral size shrinks down to ~20 μm. Similarly, the effects of densification are also reflected on the roughness of the cross-section surface. Compressed samples are increasingly denser and more compact (Figure 1b,c) than untreated reed (Figure 1a). The roughness, quantified as the root mean square of the height, is reduced by 7-fold, from 2.68 to 0.36 μm after densification. This reduction is mostly due to partial removal of the lignin that accounts for the soft part [36,37] of the untreated reed matrix while, in the densified samples, stiff cellulose microfibrils (CMFs) become the predominant component [36,37]. As already noted for the collapse of parenchyma structures, thermo-compression represents a partial treatment. Indeed, the roughness is slightly reduced, from 2.68 to 2.44 μm.
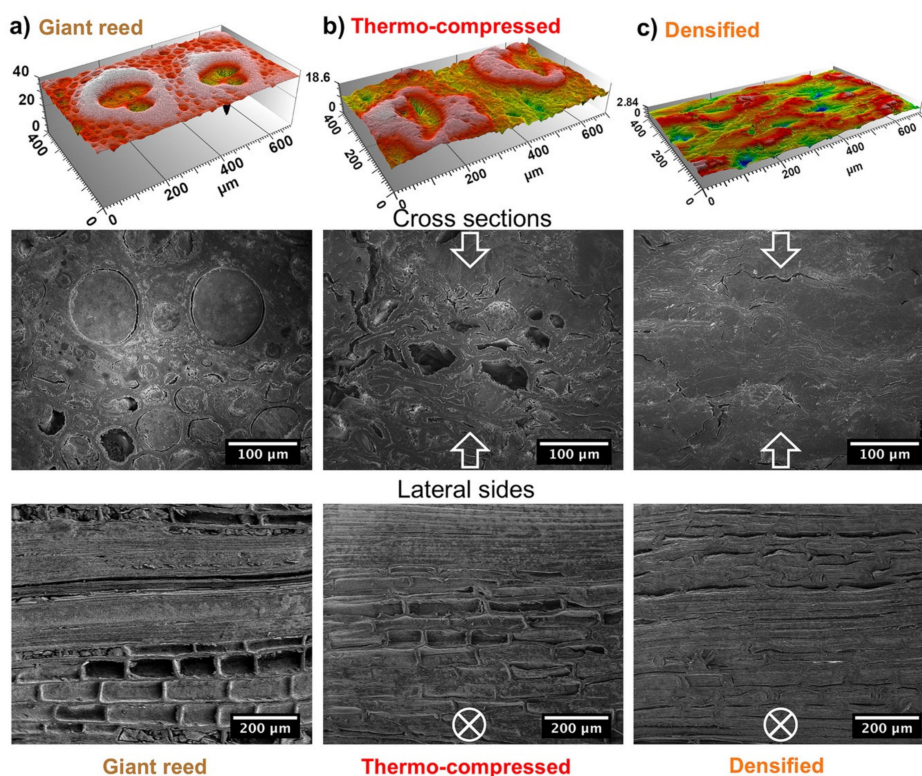
Figure 1. The first row of images shows the cross-section morphologies of (**a**) R, (**b**) TC, (**c**) D samples obtained by profilometry analysis. The second and third rows show SEM images of the cross sections and the lateral sides of (**a**) R, (**b**) TC, (**c**) D. White arrows in SEM images show the direction of applied pressure in the thermo-compression treatment.

As just discussed, the different treatments have an effect on the structure of materials, and they involve a density change. The different mass densities are 0.468 ± 0.015, 0.804 ± 0.086, 1.259 ± 0.010, 1.265 ± 0.035, 1.279 ± 0.031 g/cm^3 for R, TC, D, D + GO and D + SiC specimens, respectively. It is worthy of attention that the density of D sample is still lower than that of cellulose [38], which ideally corresponds to a complete densification and lignin removal. In fact, lignin is not completely removed in D and there are still some voids after densification. Moreover, the densification treatment has proven to be very effective in the packing of internal structures since the density of D is 8% higher than single reed fibers [6]. The lower packing density of TC compared to D is due to the lack of the lignin removal process, which does not allow to achieve high levels of compaction during thermo-compression.

SEM images (Figure 1) give a clear focus on the various extents of collapse associated with the different treatments that were performed. The first row of SEM images shows the cross sections, the second row shows the lateral side parallel to CMFs. The collapse in the internal structures increases going from left (R) to right (TC, D). We found that the densified reed (Figure 1c) has a far more compact and ordered structure than natural reed, but there is still a presence of some voids between CMFs, which are of approximately several microns long and hundreds of nanometers thick. Both the compact structure and the presence of small voids have a crucial importance for the intercalation of nanoparticles and the formation of intermolecular interactions, such as hydrogen bonding, with the surrounding CMFs.

By comparing SEM micrographs of TC and D (Figure 1b,c), it can be clearly seen that TC is less dense than D, while TC is still maintaining a structure similar to R. This resemblance disappears in D, D + GO, and D + SiC (Figure 2a) where the structural features of R cannot be distinguished anymore.

This similarity disappears in D, D + GO, and D + SiC where the structural characteristics of R are no longer observable. Figure 2a shows cross-section SEM images of the D, D + GO, and D + SiC

samples, at various magnifications. SiC nanoparticles and GO flakes filled the voids in the D sample (Figure 2a), as initially supposed, forming thin layers at the interface between CMFs.
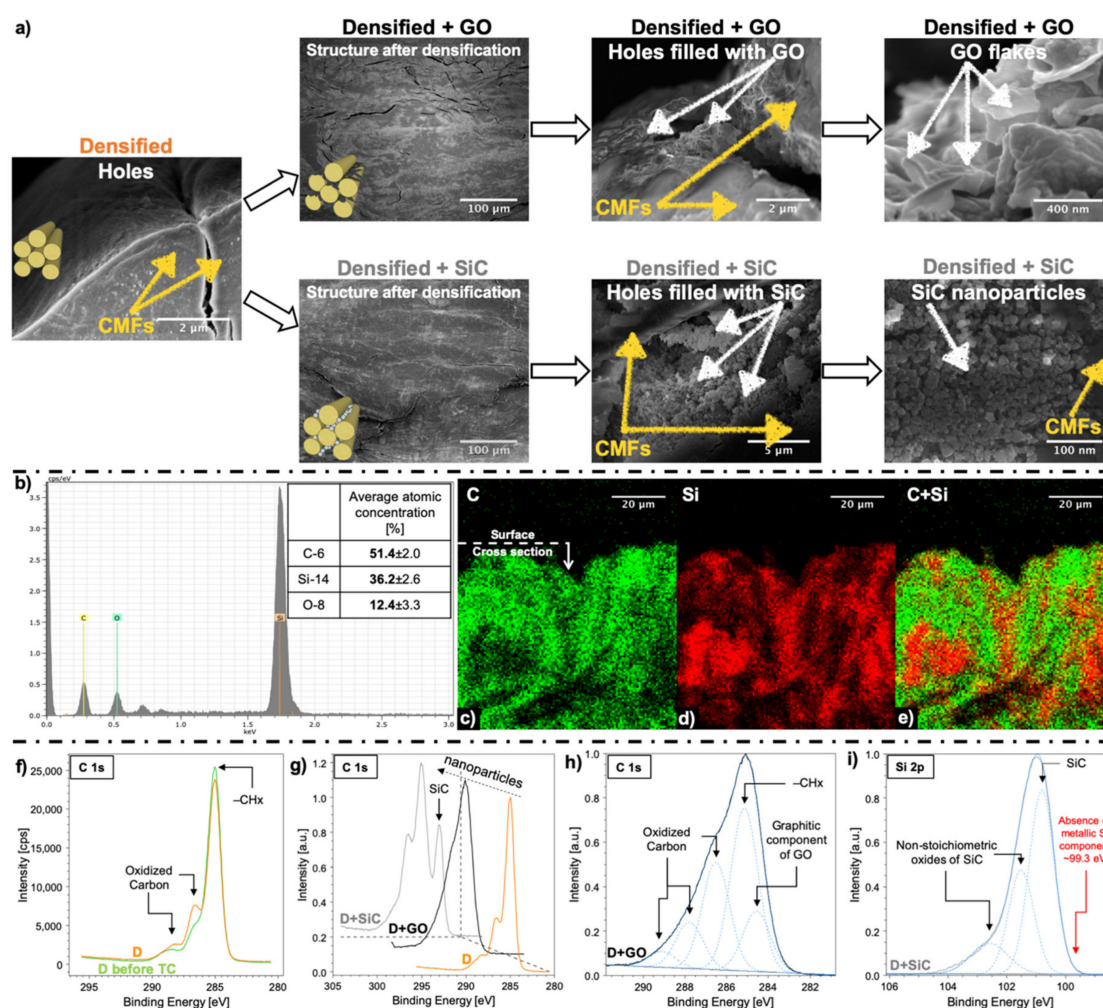
Figure 2. (**a**) SEM images of D, D+GO and D+SiC specimens. The second column displays the D + GO and D + SiC samples after nanoparticles intercalation and densification treatments: There is no evident morphological difference between the two. The third and fourth columns show high magnification SEM images with details of the location of SiC nanoparticles and GO flakes at the interface of cellulose microfibrils (CMFs). GO, SiC, and CMFs are highlighted with arrows. (**b**) EDX spectrum performed at 10 keV. The table reports the average quantitative elemental analysis of carbon (C), silicon (Si), oxygen (O) from three different wide scans sampled next to the surface in SiC-rich regions. Maps of the atomic percentage of the cross-section of D + SiC specimens: (**c**) C, (**d**) Si, (**e**) C + Si. XPS analysis of the (**f**) thermo-compression treatment on lignin etched reed, (**g**) nanoparticles intercalation on densified reed; (**h**) GO flakes, and (**i**) SiC nanoparticles intercalation in the densified reed.

EDX analysis was carried out to investigate the distribution of silicon in the D + SiC specimens. Both atomic concentration spectra (Figure 2b) and atomic distribution maps (Figure 2c,d,e) have been collected to quantify the percentage of silicon carbide on the specimen surface and its distribution in densified giant reed as a result of SiC intercalation. As it can be seen through EDX signal, the atomic concentration of Si was about 36% at surface (Figure 2b). SiC nanoparticles penetrated the D + SiC sample through the surface and naturally their concentration at surface is higher than in the bulk (Figure 2d). Whereas a rough estimate of the concentration of nanoparticles, calculated from density changes, yields ~0.9 wt% for both D + GO and D + SiC samples.

For the other samples, EDX analysis cannot provide meaningful insights since they are mostly composed of carbon, oxygen, and hydrogen. The sensitivity of EDX technique is not enough to precisely quantify elements with such low atomic numbers. Therefore, the XPS analysis was carried out to have a broader view of the chemical composition, owing to its higher sensitivity to C and O atoms than EDX analysis and its possibility to investigate chemical bonds.

Samples after delignification and after densification were compared to evaluate the effect of the thermo-compression treatment on the material (Figure 2f). Thermo-compression induces a slight conversion of −CHx into epoxy, alkoxy, and carbonyl components (Figure 2f) in the delignified reed. We suspect that alongside delignification, there is a decrease in crystallinity of cellulose (see Figure S1), owing to the alkaline environment [39]. According to the delignification treatment optimized by Song et al. [24], which was here applied on giant reed, it revealed 12% reduction of the cellulose content, while hemicellulose was decreased 4-fold.

Figure 2g shows different bonds in densified reed after introducing the GO flakes and SiC nanoparticles. D + GO spectrum shows a graphitic shoulder at binding energies lower than $(-CH_x)$ bonds. As well as, an increase in all the oxidized carbon components (C–O, C=O and O=C–O) can be assumed from Figure 2h. By adding SiC nanoparticles, a new peak arises at ~283 eV, as shown in Figure 2i for the Si 2p line. Presence of GO flakes, when compared to D spectrum (Figure 2g), generates a significant increment of all the oxidized carbon components (Figure 2h) in the overall structure of densified reed. There is also the rise of a graphitic shoulder ~284.6 (Figure 2h) owing to the molecular structure of GO flakes. The Si^0 component, which should fall at ~99.3 eV (Figure 2i), is absent and the narrow peak of SiC (Figure 2i) demonstrates that SiC nanoparticles are crystalline. In addition, some native oxides are formed on the surface of SiC nanoparticles, as denoted by the presence of the nonstoichiometric oxide components in the Si 2p XPS spectrum (Figure 2i).

The evaluation of treatments' effect on the mechanical properties are analyzed in this section. The stress-strain curves of the uniaxial tension test are reported in Figure 3a,b. It is worthy of attention that flexural properties follow the same trend of tensile tests, as shown in Figure 3.

All samples exhibit a brittle behavior. D, D + GO, D + SiC display a mostly linear loading curve, typical of natural fibers with high cellulose content [40]. Non chemically-treated samples, which have higher lignin concentration, show a nonlinear loading curve at low strains linked to the progressive loading of cellulose fibers through the deformation of cell walls [6] followed by a viscoelastic response, whose contribution mainly depends on amorphous regions (lignin, hemicelluloses, pectins) [6,41].

From the stress-strain curves (Figure 3a) we computed a Young's modulus for the giant reed of 4.5 GPa (Figure 3c), which agrees with the measurements of Speck et al. [42]. After densification, stiffness rises to 11.9 ± 1.1 GPa and likewise the tensile and flexural strengths results in a drastic improvement of 3.66 times for the tensile strength (from 64 ± 4 MPa in R to 234 ± 26 MPa in D, Figure 3d) and 2.15 times for flexural strength (from 108 ± 5 to 232 ± 4 MPa, Figure 3e). Hence, the obtained performance of densified reed is superior to regenerated cellulose films [43] and very similar to both those of isolated reed fibers [6] and cellulose nanopaper [11]. Moreover, the properties achieved through densification are superior to many types of bamboo [7,16,44], resulting in a highly competitive construction material (Figure 3g,h).

Introducing nanomaterials grants an additional boost to the performance of densified reed. Indeed, the Young's modulus rises to 12.3 ± 1.0 for D + GO and 14.0 ± 1.1 GPa for D + SiC (Figure 3c), which are higher than most engineering polymers (Figure 3g). Therefore, these materials moved from the wood's group in the Ashby chart (Figure 3g) to engineering composites. Accordingly, both tensile strength (+ 13% for GO and + 30% for SiC) and flexural strength (+ 5% for GO and + 15% for SiC) are improved (Figure 3d,e). These enhancements in mechanical properties are caused by the addition of nanomaterials, which improves the interfacial adhesion between CMFs. Densified nanocomposites fall into the density category of biological materials designed to work under tension, such as tendons, but they show higher strength. As expected, the upper limit in terms of both density and strength for the

nanocomposites is cellulose [17,45], which is the strongest structural component of reed. However, their strength is superior to wood and plywood (Figure 3h).
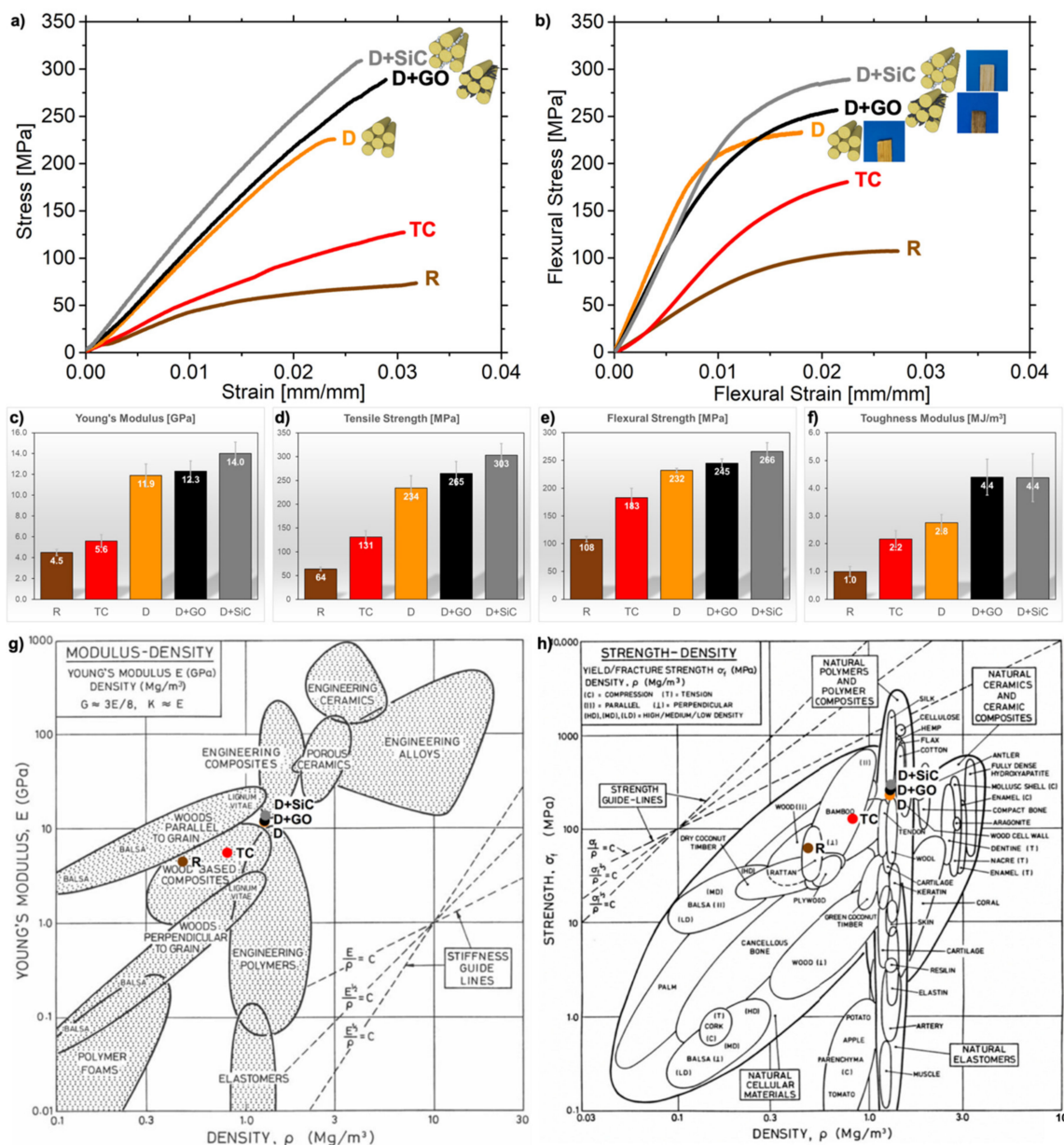
Figure 3. Average representative (**a**) stress-strain and (**b**) flexural stress-strain curves. Simplified representation of CMFs with GO flakes and SiC nanoparticles is given for D, D + GO, D + SiC. After the addition of nanoparticles, samples' color change as shown (D + GO veers towards black while D + SiC veers towards gray). Histograms summarizing the properties of R, TC, D, D + GO, and D + SiC samples: (**c**) Young's modulus, (**d**) tensile strength, (**e**) flexural strength, and (**f**) toughness modulus (area under the tensile stress-strain curve). Error bars represent the standard deviation. Material properties charts show the five materials of this work compared to common engineering materials: (**g**) Young's modulus vs. density chart and (**h**) strength vs. density chart - adapted from [17] with permission. In the Ashby charts, the final densified products sit above the strength and stiffness guidelines traced using reed as the reference point.

Nanoparticles improved the deformation capabilities in bending (+ 10% for D + GO and + 20% for D + SiC, see Figure S2). Composite wood-like structures have a predominant deformation by shear,

which is concentrated in the soft matrix [46], rather than on the stiffer cellulose fibers. It is clear that, with a partial removal of the lignin and hemicellulose matrix, the deformation capabilities of reed are reduced [47]. Indeed, densified reed exhibits lowered strain to failure in both tensile and flexural tests (see Figure S2). However, the intercalation of nanoparticles generates a remarkable increase of the materials' toughness modulus (Figure 3f). It goes from 2.8 MJ/m^3 after densification, which is the current state-of-the-art process, to 4.4 MJ/m^3 for D + GO and D + SiC.

To further compare the mechanical properties of each material, specific toughness modulus was taken into account. It is calculated by dividing the area under stress strain curves (i.e., toughness modulus) by the density. As a result of the variations in packing density introduced by the treatments, specific toughness modulus is suitable to evaluate the intrinsic improvements in toughening efficiency rather than toughness modulus. This is due to the increase in the packing density induced by compression, owing to a toughness modulus increase while the specific toughness modulus remains the same.

No marked difference in specific toughness modulus (see Figure S2) surfaces in the three samples of R, TC and D. Instead, the intercalation of nanoparticles acts as a further reinforcement on top of the previous densification treatments as it generates an improvement in the specific toughness moduli of +59% for D + GO and +56% for D + SiC (Figure S2). The toughening could be caused by the location of nanoparticles at the interface between CMFs (Figure 2a). Indeed, both SiC nanoparticles and GO flakes were intercalated into the pores of giant reed, which were opened through chemical treatment and then closed by thermo-compression (Figure 1, Figure 2a). It can be interpreted in terms of better interfacial adhesion or increased in the chemical cross-linking at the interface driven by the additional hydrogen bonds available from the GO structure [48,49] and the nonstoichiometric oxides shell (Figure 2i) on SiC nanostructures [50,51]. Not to mention that the small amount of Ca impurities, which was found in all the samples (see Figure S1), was reported to have a beneficial effect on the chemical cross-linking between GO and cellulose [52], thus effectively enhancing the stiffness and the strength between GO layers [53]. It was also demonstrated that the densification process on wood at moderately high temperatures can lead to the formation of new hydrogen bonds between CMFs [12,24], which is here favored by a high degree nanofibers' alignment. The higher level of oxidation emerging from XPS analysis (Figure 2f) and the formation of new hydrogen bonds leads to a highly densified material that is stronger than the same sample compressed at room temperature.

As a result of the intercalation of nanoparticles, we estimated an average improvement of the interfacial fracture energy between CMFs that is 1.28 ± 0.33 for D + GO and 1.47 ± 0.36 for D + SiC, both compared to the D sample (see Supplementary). The fracture energy was calculated according to an analytical model [54] and it is proportional to $\sigma^2/(E*R)$, where σ is the tensile strength, E is the Young's modulus of the material, and R is the radius of the CMFs.

Two different tests were performed to evaluate the burning resistance of the samples: A free flame burning test and a thermo-indentation. A modified Taghiyari method [28] was used to perform the free flame burning test (Figure 4a).

Figure 4b shows the comparison between all the samples. The normalized burned volume is calculated as reported in the Methods section. During the first half of the test the reed burns faster than its compressed and densified counterparts, then it auto-extinguishes itself faster than the TC sample. Regarding the overall resistance to free flame, the densification treatment yields the best results as it performs almost twice better than all other samples.

All samples showed fire extinguishing properties (Figure 4b). The only exception is D + GO. After about 20 s, where all curves start to slow down, the specific burned volume of D + GO accelerates again. This effect cannot be entirely attributed to the high thermal conductivity of GO. In fact, differential scanning calorimetry (DSC) and thermogravimetric analysis TGA curves of GO[48] show a strong exothermic reaction at about 200 °C, the energy release associated with it can drive flame propagation and accelerate the burning of the sample depicted by the black line in Figure 4b. Furthermore, the Na impurities that remain in the structure after the delignification process (see XPS spectra in Figure S1)

interact with GO flakes to accelerate the burning mechanism [55,56]. In general, the introduction of nanoparticles seems to reduce the flame retarding properties that the D shows compared to the R samples.
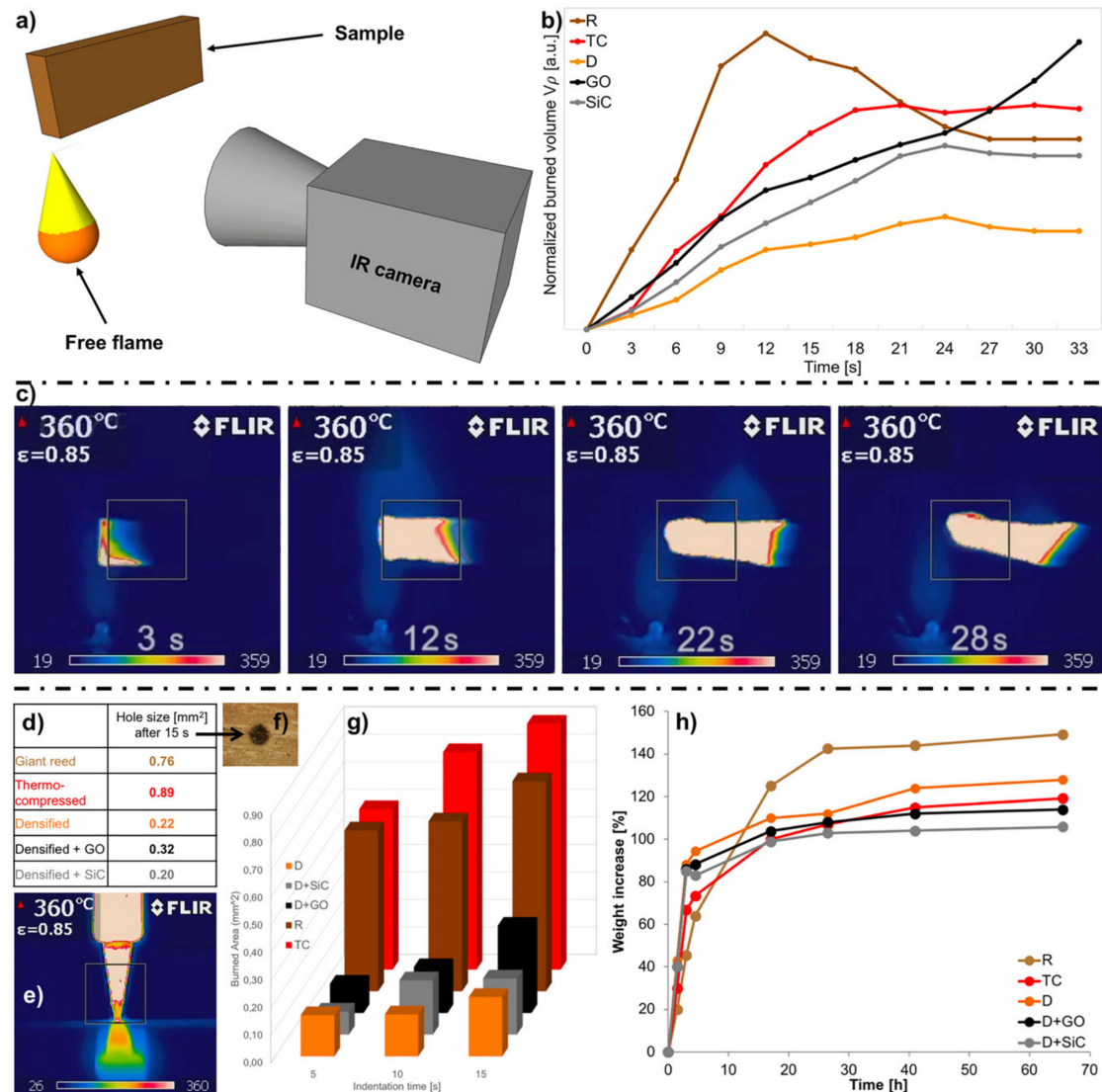
Figure 4. (**a**) Schematic representation of the burning test setup. (**b**) Burning test results of all specimen types. (**c**) Time evolution of thermal imaging data from D + GO sample (complete videos are available in SI). (**d**) Table showing the burned area after the 15 s of thermo-indentation (**e**) thermographic image of the indenter tip (**f**) burned area results of all specimens when subjected to 5, 10, and 15 s of thermo-indentation (**g**) burned area vs. indentation time. (**h**) Accelerated humidity absorption tests carried out on R, TC, D, D + GO, and D + SiC specimens. The graph represents the weight increase of samples vs. exposition time at constant 97% of relative humidity.

Ignition of wood can result from free flame or contact with a hot body. An ad-hoc thermo-indentation test was designed to quantify the resistance of each sample to burn in contact with a hot body.

The thermo-indentation was performed using a hot tip perpendicular to the surface (Figure 4e). The burned area from the tip was used to evaluate the data (Figure 4f). These measurements depend both on the specific burning features of the samples and on the elastic modulus of the surface of the indented sample. The thermo-indentation performance can be explained cross comparing the data

of the specific burning test with the elastic modulus. In fact, both R and TC have higher indentation area and TC shows a higher burned area compared to R (Figure 4g). Furthermore, the densified and nanocomposite reed have a lower burned area than both TC and R, due to higher burning resistance and higher Young's modulus of D, D+GO and D+SiC (Figures 4g and 3c), which increase thermo-indentation performance. Moreover, also during the thermo-indentation of the densified sample with GO nanoparticles, the burned area saw an upright increment from 10 to 15 s that did not arise in the other samples (Figure 4g). In conclusion, both graphs of free flame and thermo-indentation show similar trends, apart from D + GO in the burning test due to the aforementioned effect (Figure 4b,c). All densified samples showed superior resistance to thermo-indentation compared to R or TC, with D + SiC having the best resistance of all for longer times (Figure 4g).

The humidity absorption characteristics of the reed samples were calculated by the percentage of weight gain at different times. Interestingly, the humidity absorption kinetics differs with the treatments applied (Figure 4h). The two samples that contain all the lignin (R, TC) have a slower initial growth but have a high final steady state. The presence of lignin has a crucial impact on the water absorption since it is a cross-linked phenolic polymer with few terminal hydroxyl groups and low water solubility [39]. Therefore, when lignin is removed (D, D + GO, D + SiC), the water gain is faster but has a lower final asymptote. This finding is correlated with the higher packing density of cellulose microfibrils in densified samples and with the increased capillarity effect that is induced by the chemical treatment [57].

The asymptotic values, which samples approximately reach after 40 h, have a maximum value of + 150% for R that has the highest moisture absorption whereas they are significantly lower when nanoparticles are added: 114% for D + GO and 106% for D + SiC. The latter ranks as the lowest absorbing specimen (Figure 4h).

In real-life scenarios the overall absorbed water is the key factor for the survival of wood and reed in critical environments. Less absorbed water will result in lower fungus development [34] and lower degradation in mechanical properties [16]. Thus, densified nanocomposite specimens will perform better under these conditions.

4. Conclusions

In this work, we presented an innovative and simple nano-reinforcing treatment for wood-like specimens that involves densification of cellulose fibrils combined with intercalation of GO and SiC nanoparticles. In particular, the process was here tested to improve the mechanical properties of an invasive plant, giant reed, into a stronger and tougher engineering composite and can be applied to other cellulose-based materials such as wood and bamboo.

Morphological and structural characterizations, performed by using profilometer, SEM, EDX, and XPS techniques, highlighted that the treatment performed intercalated the nanoparticles inside the densified giant reed. Although, nanoparticles led to no apparent influence on the structure of the densified reed, their presence and location at the interface of CMFs resulted in a better interfacial adhesion and overall improvement in mechanical performance, both for tensile and flexural properties. Indeed, the mechanical properties of the nanocomposite increase with respect to both the untreated and densified reed. The nanocomposite modified giant reed has a 1/15 of the elastic modulus and more than 1/2 of the strength of mild steel while having just 1/7 of its density. Further analysis highlighted that the nanoparticle intercalation in the densified reed enhanced the specific toughness modulus while this does not occur with the densification treatment alone. This result is due to the role played by nanoparticles during the relative sliding between cellulose microfibrils inside the material. A mechanical effect coupled with an increase in the chemical interaction could be at the root of this phenomenon. Indeed, the densification treatment involves the formation of a high number of hydrogen bonds between CMFs. The amount of these bonds could further increase by adding nanoparticles in the voids of the densified structure, especially with GO, which is rich in hydroxyl and carbonyl groups in its surface. Additionally, an increase in adhesion energy, that was estimated to

be higher for SiC nanoparticles than GO, could induce an increase stress transfer between cellulose microfibrils. Further investigations were performed to evaluate thermo-indentation and burning response of the materials. SiC and GO-densified giant reed have strongly increased fire-retarding and thermo-indentation resistances compared to the native reed. Moreover, the addition of nanoparticles in the densified reed resulted in a reduced water uptake, which can decrease its bio-deterioration and thus guarantee a longer lifespan when applied as a structural material. The versatility of this innovative treatment can be exploited to improve the mechanical properties of any kind wood-like structure. In conclusion, the nano-reinforcing densification treatment proposed in this work sheds a new insight into the possible enhancements of timber properties.

References

1. Huo, X.; Yu, A.T. Analytical review of green building development studies. *J. Green Build.* **2017**, *12*, 130–148. [CrossRef]

2. Wang, L.; Toppinen, A.; Juslin, H. Use of wood in green building: A study of expert perspectives from the UK. *J. Clean. Prod.* **2014**, *65*, 350–361. [CrossRef]

3. Kalia, S.; Kaith, B.; Kaur, I. Pretreatments of natural fibers and their application as reinforcing material in polymer composites—A review. *Polym. Eng. Sci.* **2009**, *49*, 1253–1272. [CrossRef]

4. Fridley, K.J. Wood and wood-based materials: Current status and future of a structural material. *J. Mater. Civ. Eng.* **2002**, *14*, 91–96. [CrossRef]

5. Yu, W.; Chung, K.; Chan, S. Column buckling of structural bamboo. *Eng. Struct.* **2003**, *25*, 755–768. [CrossRef]

6. Fiore, V.; Scalici, T.; Valenza, A. Characterization of a new natural fiber from *Arundo donax* L. as potential reinforcement of polymer composites. *Carbohydr. Polym.* **2014**, *106*, 77–83. [CrossRef]

7. Mahdavi, M.; Clouston, P.; Arwade, S. Development of laminated bamboo lumber: Review of processing, performance, and economical considerations. *J. Mater. Civ. Eng.* **2010**, *23*, 1036–1042. [CrossRef]

8. Simonson, C.J.; Salonvaara, M.; Ojanen, T. The effect of structures on indoor humidity—Possibility to improve comfort and perceived air quality. *Indoor Air* **2002**, *12*, 243–251. [CrossRef]

9. González-García, S.; Silva, F.J.; Moreira, M.T.; Pascual, R.C.; Lozano, R.G.; Gabarrell, X.; Pons, J.R.; Feijoo, G. Combined application of LCA and eco-design for the sustainable production of wood boxes for wine bottles storage. *Int. J. Life Cycle Assess.* **2011**, *16*, 224–237. [CrossRef]

10. Hillring, B. World trade in forest products and wood fuel. *Biomass Bioenergy* **2006**, *30*, 815–825. [CrossRef]

11. Zhu, H.; Xiao, Z.; Liu, D.; Li, Y.; Weadock, N.J.; Fang, Z.; Huang, J.; Hu, L. Biodegradable transparent substrates for flexible organic-light-emitting diodes. *Energy Environ. Sci.* **2013**, *6*, 2105–2111. [CrossRef]

12. Huang, J.; Zhu, H.; Chen, Y.; Preston, C.; Rohrbach, K.; Cumings, J.; Hu, L. Highly transparent and flexible nanopaper transistors. *ACS Nano* **2013**, *7*, 2106–2113. [CrossRef] [PubMed]

13. Ramage, M.H.; Burridge, H.; Busse-Wicher, M.; Fereday, G.; Reynolds, T.; Shah, D.U.; Wu, G.; Yu, L.; Fleming, P.; Densley-Tingley, D.; et al. The wood from the trees: The use of timber in construction. *Renew. Sustain. Energy Rev.* **2017**, *68*, 333–359. [CrossRef]

14. Joseph, P.; Tretsiakova-McNally, S. Sustainable non-metallic building materials. *Sustainability* **2010**, *2*, 400–427. [CrossRef]

15. Ghavami, K. Bamboo as reinforcement in structural concrete elements. *Cem. Concr. Compos.* **2005**, *27*, 637–649. [CrossRef]

16. Sharma, B.; Gatóo, A.; Bock, M.; Ramage, M. Engineered bamboo for structural applications. *Constr. Build. Mater.* **2015**, *81*, 66–73. [CrossRef]

17. Wegst, U.; Ashby, M. The mechanical efficiency of natural materials. *Philos. Mag.* **2004**, *84*, 2167–2186. [CrossRef]

18. Coffman, G.C. Factors Influencing Invasion of Giant Reed (*Arundo donax*) in Riparian Ecosystems of Mediterranean-Type Climate Regions. Ph.D. Thesis, University of California, Los Angeles, CA, USA, 2007.

19. Rüggeberg, M.; Burgert, I.; Speck, T. Structural and mechanical design of tissue interfaces in the giant reed *Arundo donax*. *J. R. Soc. Interface* **2009**, *7*, 499–506. [CrossRef]

20. Spatz, H.-C.; Beismann, H.; Brüchert, F.; Emanns, A.; Speck, T. Biomechanics of the giant reed *Arundo donax*. *Philos. Trans. R. Soc. Lond. B Biol. Sci.* **1997**, *352*, 1–10. [CrossRef]

21. Perdue, R.E. *Arundo donax*—Source of musical reeds and industrial cellulose. *Econ. Bot.* **1958**, *12*, 368–404. [CrossRef]

22. Angelini, L.G.; Ceccarini, L.; Bonari, E. Biomass yield and energy balance of giant reed (*Arundo donax* L.) cropped in central Italy as related to different management practices. *Eur. J. Agron.* **2005**, *22*, 375–389. [CrossRef]

23. Salvati, E.; Brandt, L.R.; Uzun, F.; Zhang, H.; Papadaki, C.; Korsunsky, A.M. Multiscale analysis of bamboo deformation mechanisms following NaOH treatment using X-ray and correlative microscopy. *Acta Biomater.* **2018**, *72*, 329–341. [CrossRef] [PubMed]

24. Song, J.; Chen, C.; Zhu, S.; Zhu, M.; Dai, J.; Ray, U.; Li, Y.; Kuang, Y.; Li, Y.F.; Quispe, N.; et al. Processing bulk natural wood into a high-performance structural material. *Nature* **2018**, *554*, 224. [CrossRef] [PubMed]

25. Rassam, G.; Ghofrani, M.; Taghiyari, H.R.; Jamnani, B.; Khajeh, M.A. Mechanical performance and dimensional stability of nano-silver impregnated densified spruce wood. *Eur. J. Wood Wood Prod.* **2012**, *70*, 595–600. [CrossRef]

26. Li, J.; Zheng, H.; Sun, Q.; Han, S.; Fan, B.; Yao, Q.; Yan, C.; Jin, C. Fabrication of superhydrophobic bamboo timber based on an anatase TiO_2 film for acid rain protection and flame retardancy. *RSC Adv.* **2015**, *5*, 62265–62272. [CrossRef]

27. Li, J.; Sun, Q.; Yao, Q.; Wang, J.; Han, S.; Jin, C. Fabrication of robust superhydrophobic bamboo based on ZnO nanosheet networks with improved water-, UV-, and fire-resistant properties. *J. Nanomater.* **2015**, *431426*. [CrossRef]

28. Taghiyari, H.R.; Rangavar, H.; Nouri, P. Fire-retarding properties of nanowollastonite in MDF. *Eur. J. Wood Wood Prod.* **2013**, *71*, 573–581. [CrossRef]

29. Tjong, S.C. Novel nanoparticle-reinforced metal matrix composites with enhanced mechanical properties. *Adv. Eng. Mater.* **2007**, *9*, 639–652. [CrossRef]

30. Rodgers, R.M.; Mahfuz, H.; Rangari, V.K.; Chisholm, N.; Jeelani, S. Infusion of SiC nanoparticles into SC-15 epoxy: An investigation of thermal and mechanical response. *Macromol. Mater. Eng.* **2005**, *290*, 423–429. [CrossRef]

31. Kisku, S.K.; Satyabrata, D.; Sarat, K.S. Dispersion of SiC nanoparticles in cellulose for study of tensile, thermal and oxygen barrier properties. *Carbohydr. Polym.* **2014**, *99*, 306–310. [CrossRef]

32. Gao, W. The Chemistry of Graphene Oxide. In *Graphene Oxide*; Springer: Cham, Switzerland, 2015; pp. 61–95.

33. Huang, Q.; Xu, M.; Sun, R.; Wang, X. Large scale preparation of graphene oxide/cellulose paper with improved mechanical performance and gas barrier properties by conventional papermaking method. *Ind. Crops Prod.* **2016**, *85*, 198–203. [CrossRef]

34. Zhang, X.; Yu, H.; Huang, H.; Liu, Y. Evaluation of biological pretreatment with white rot fungi for the enzymatic hydrolysis of bamboo culms. *Int. Biodeterior. Biodegrad.* **2007**, *60*, 159–164. [CrossRef]

35. Scordia, D.; Cosentino, S.L.; Lee, J.W.; Jeffries, T.W. Dilute oxalic acid pretreatment for biorefining giant reed (*Arundo donax* L.). *Biomass Bioenergy* **2001**, *25*, 3018–3024. [CrossRef]

36. Hepworth, D.; Vincent, J. Modelling the mechanical properties of xylem tissue from tobacco plants (*Nicotiana tabacum* 'Samsun') by considering the importance of molecular and micromechanisms. *Ann. Bot.* **1998**, *81*, 761–770. [CrossRef]

37. Jin, K.; Qin, Z.; Buehler, M.J. Molecular deformation mechanisms of the wood cell wall material. *J. Mech. Behav. Biomed. Mater.* **2015**, *42*, 198–206. [CrossRef] [PubMed]

38. Meredith, R. *Mechanical Properties of Textile Fibres*; Interscience: New York, NY, USA, 1956.

39. Hon, D.S. *Chemical Modification of Lignocellulosic Materials*; Routledge: New York, NY, USA, 2017.

40. Symington, M.C.; Banks, W.M.; West, O.D.; Pethrick, R.A. Tensile testing of cellulose based natural fibers for structural composite applications. *J. Compos. Mater.* **2009**, *43*, 1083–1108. [CrossRef]

41. Lord, A.E. Viscoelasticity of the giant reed material *Arundo donax*. *Wood Sci. Technol.* **2003**, *37*, 177–188. [CrossRef]

42. Speck, O.; Spatz, H.C. Damped oscillations of the giant reed *Arundo donax* (*Poaceae*). *Am. J. Bot.* **2004**, *91*, 789–796. [CrossRef]

43. Yang, Q.; Fukuzumi, H.; Saito, T.; Isogai, A.; Zhang, L. Transparent cellulose films with high gas barrier properties fabricated from aqueous alkali/urea solutions. *Biomacromolecules* **2011**, *12*, 2766–2771. [CrossRef]

44. Dixon, P.G.; Gibson, L.J. The structure and mechanics of Moso bamboo material. *J. R. Soc. Interface* **2014**, *11*, 20140321. [CrossRef]

45. Mittal, N.; Ansari, F.; Gowda, V.K.; Brouzet, C.; Chen, P.; Larsson, P.T.; Roth, S.V.; Lundell, F.; Wågberg, L.; Kotov, N.A.; et al. Multiscale Control of Nanocellulose Assembly: Transferring Remarkable Nanoscale Fibril Mechanics to Macroscale Fibers. *ACS Nano* **2018**, *12*, 6378–6388. [CrossRef] [PubMed]

46. Fratzl, P.; Burgert, I.; Gupta, H.S. On the role of interface polymers for the mechanics of natural polymeric composites. *Phys. Chem. Chem. Phys.* **2004**, *6*, 5575–5579. [CrossRef]

47. Fratzl, P.; Burgert, I.; Keckes, J. Mechanical model for the deformation of the wood cell wall: Dedicated to Professor Dr. Dr. hc Franz Jeglitsch on the occasion of his 70th birthday. *Z. Met.* **2004**, *95*, 579–584. [CrossRef]

48. Compton, O.C.; Cranford, S.W.; Putz, K.W.; An, Z.; Brinson, L.C.; Buehler, M.J.; Nguyen, S.T. Tuning the mechanical properties of graphene oxide paper and its associated polymer nanocomposites by controlling cooperative intersheet hydrogen bonding. *ACS Nano* **2012**, *6*, 2008–2019. [CrossRef]

49. Tripathi, M.; Mahmood, H.; Novel, D.; Iacob, E.; Vanzetti, L.; Bartali, R.; Speranza, G.; Pegoretti, A.; Pugno, N. Nanoscale friction of graphene oxide over glass-fibre and polystyrene. *Compos. Part B Eng.* **2018**, *148*, 272–280. [CrossRef]

50. Önneby, C.; Pantano, C. Silicon oxycarbide formation on SiC surfaces and at the SiC/SiO_2 interface. *J. Vac. Sci. Technol. A Vac. Surf. Films* **1997**, *15*, 1597–1602. [CrossRef]

51. Gaiardo, A.; Fabbri, B.; Giberti, A.; Valt, M.; Gherardi, S.; Guidi, V.; Malagù, C.; Bellutti, P.; Pepponi, G.; Casotti, D.; et al. Tunable formation of nanostructured SiC/SiOC core-shell for selective detection of SO_2. *Sens. Actuators B Chem.* **2020**, *305*, 127485. [CrossRef]

52. Liu, Y.-T.; Feng, Q.-P.; Xie, X.-M.; Ye, X.-Y. The production of flexible and transparent conductive films of carbon nanotube/graphene networks coordinated by divalent metal (Cu, Ca or Mg) ions. *Carbon* **2011**, *49*, 3371–3375. [CrossRef]

53. Park, S.; Lee, K.-S.; Bozoklu, G.; Cai, W.; Nguyen, S.T.; Ruoff, R.S. Graphene oxide papers modified by divalent ions—Enhancing mechanical properties via chemical cross-linking. *ACS Nano* **2008**, *2*, 572–578. [CrossRef]

54. Pugno, N.; Carpinteri, A. Tubular adhesive joints under axial load. *J. Appl. Mech.* **2003**, *70*, 832–839. [CrossRef]

55. McAllister, M.J.; Li, J.-L.; Adamson, D.H.; Schniepp, H.C.; Abdala, A.A.; Liu, J.; Herrera-Alonso, M.; Milius, D.L.; Car, R.; Prud'homme, R.K.; et al. Single sheet functionalized graphene by oxidation and thermal expansion of graphite. *Chem. Mater.* **2007**, *19*, 4396–4404. [CrossRef]

56. Shi, Y.; Li, L.-J. Chemically modified graphene: Flame retardant or fuel for combustion? *J. Mater. Chem.* **2011**, *21*, 3277–3279. [CrossRef]

57. Pejic, B.M.; Kostic, M.M.; Skundric, P.D.; Praskalo, J.Z. The effects of hemicelluloses and lignin removal on water uptake behavior of hemp fibers. *Bioresour. Technol.* **2008**, *99*, 7152–7159. [CrossRef] [PubMed]

1 SUPPLEMENTARY MATERIALS

2 Strengthening of Wood-like Materials via
3 Densification and Nanoparticle Intercalation

4 **David Novel [1,2], Simone Ghio [1,2], Andrea Gaiardo [2,3], Antonino Picciotto [2], Vincenzo Guidi [3],**

5 **Giorgio Speranza [2,4,5], Maurizio Boscardin [2], Pierluigi Bellutti [2], Nicola M. Pugno[1,6,7,*]**

6   1 Laboratory of Bio-Inspired, Bionic, Nano, Meta Materials & Mechanics, Department of Civil, Environmental
7   and Mechanical Engineering, University of Trento, Via Mesiano 77, I-38123, Trento, Italy
8   2 Centre for Materials and Microsystems, Fondazione Bruno Kessler, via Sommarive 18, I-38123 Trento, Italy
9   3 Department of Physics and Earth Science, University of Ferrara, Via Saragat 1/c, I-44122 Ferrara, Italy
10   4 Istituto di Fotonica e Nanotecnologie & Consiglio Nazionale delle Ricerche IFN - CNR, via alla Cascata 56/C
11   Povo, I-38123 Trento, Italy
12   5 Department of Industrial Engineering, University of Trento, v. Sommarive 9, I-38123 Trento, Italy
13   6 School of Engineering and Materials Science, Queen Mary University of London, Mile End Road, London,
14   E1 4NS, United Kingdom
15   7 Ket Labs, Edoardo Amaldi Foundation, Via del Politecnico snc, I-00133, Rome, Italy

16 **Note 1 - XPS:**
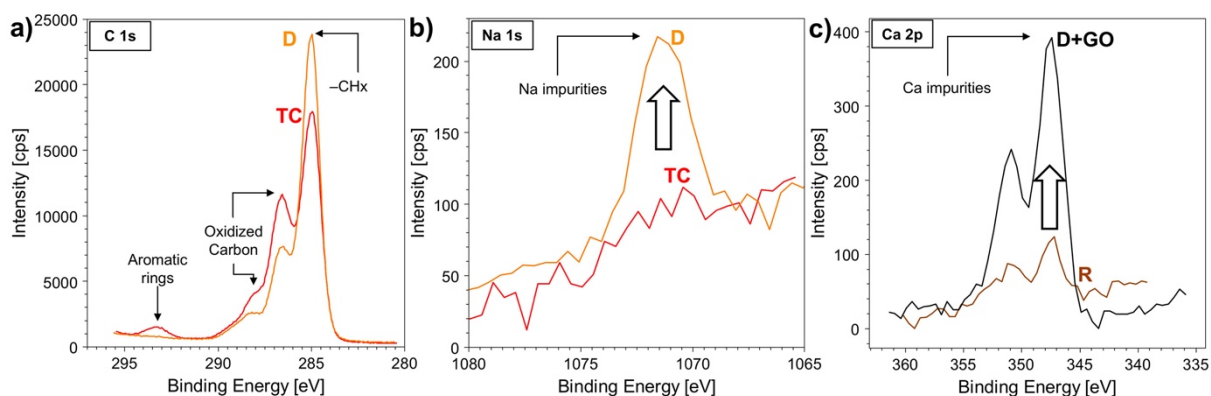
18 **Figure S1.** a) The difference in XPS spectra between TC and D shows the effects of delignification. TC
19 and D samples differs only for the delignification process. b) presence of Na impurities. They are
20 increased after the chemical etching c) presence of Ca impurities. They are increased from <0.1% to
21 ~0.5% after the chemical etching. Ca impurities have an important effect on the D+GO as they interact
22 with GO during burning.

23   The binding energy that is associated with the structure at ~294.3 eV in the C1s spectrum of "TC"
24 in Fig. S1 has energies that are too high to justify the bonding of carbon with any element. It could
25 instead be explained with a shake-up structure that is formed due to the presence of aromatic rings.
26 This structure appears only in R and TC, and it disappears in all the other specimens, which were
27 subject to delignification process. Thus, it could arise from the aromatic rings in the molecular
28 structure of lignin [1]. As Fig. S1 shows, delignification took place going from TC to D and this
29 corresponds with the decrease of the structure at ~294.3 eV. However, the decrease of this feature is
30 not enough to explain the increase of the component associated with –CH$_x$ at 285.5 eV [2] to the
31 detriment of the oxidized carbon that occurs as a result of the chemical delignification process.
32   A possible concurrent phenomenon is the degradation of hemicellulose and cellulose [3]. Indeed,
33 alkaline treatments on wood-like materials remove part of the lignin and partially depolymerize
34 hemicellulose and cellulose [4]. The subsequent degradation is turned into an extraction of the

35   different sugars forming hemicellulose or the glucose from cellulose. In particular, in solutions with
36   increased alkalinity, the extraction of glucose from the depolymerization of cellulose in natural fibers
37   is increased [5]. This extraction can reduce the overall amount of oxidized carbons.

Note 2 - Mechanical properties:
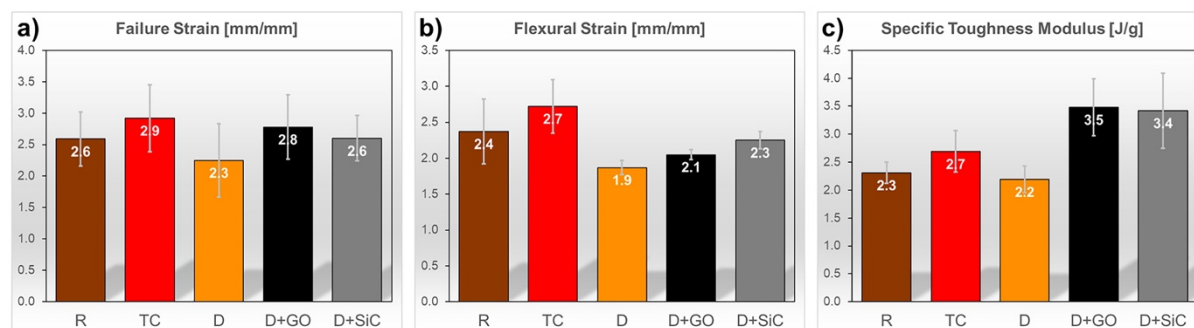
Figure S2. Histograms summarizing the mechanical properties of R, TC, D, D+GO and D+SiC
samples: a) failure strain, b) flexural strain and c) specific toughness modulus, which was derived
from the toughness modulus as described in the article. Error bars represent the standard deviation.

Note 3 - Interfacial fracture energy:

44   As for wood-like structures, the mechanical performance of densified and composite reed is
45   dominated by the shear load transfer between cellulose microfibrils [6].
46   Thus, failure mechanics is prevalently governed by the shear failure at interfibrillar interface.
47   Griffith linear elastic fracture mechanics have proven to be suitable describing the failure of adhesive
48   joints subjected to complex loading conditions [7, 8]. It was suggested [9] that there is a correlation
49   between the load necessary for the crack to propagate and the fracture energy of the interface joint.
50   This insight could result in a better understanding of the adhesion in our nanocomposite materials.
51   The microscale interactions between nanoparticles and cellulose microfibrils can be treated within a
52   precise geometrical configuration that is modelled to estimate the increase in toughness reported after
53   the introduction of nanoparticles. We can imagine the interface as an adhesive joint that unbinds
54   when crack propagates. Fig. S2 shows a hypothetical loading setup for a group of fibrils in mutual
55   contact. An isotropic linear elastic behavior is assumed for the materials involved, i.e. CMFs and
56   interface materials. If the adhesive layer thickness h tends to zero, then the elastic strain energy
57   absorbed by the layer is negligible. A full analytical derivation was proposed [9] for a similar
58   geometry of concentric tubes joined by an adhesive at their interface and subjected to axial load. The
59   link between critical load for crack propagation, adhesion and geometry holds to be:

$$N_c = \sqrt{4\pi R G_a \frac{E_2 A_2}{E_1 A_1}(E_1 A_1 + E_2 A_2)} \quad (1)$$

61   where A_i are cross-section areas, E_i are Young's moduli and their product represent the axial rigidity
62   of tubular elements in tension and the internal element have radius R (Fig. S3a). N_c is the critical load
63   for which the critical strain energy release rate G_a is reached. Eq.1 is applied to bodies #1, #2 in Fig.
64   S3a where the body #2 is cylindrical and it could be extended to a modified configuration shown in
65   Fig. S3b that resembles to the CMFs structure of D, D+GO and D+SiC.

66
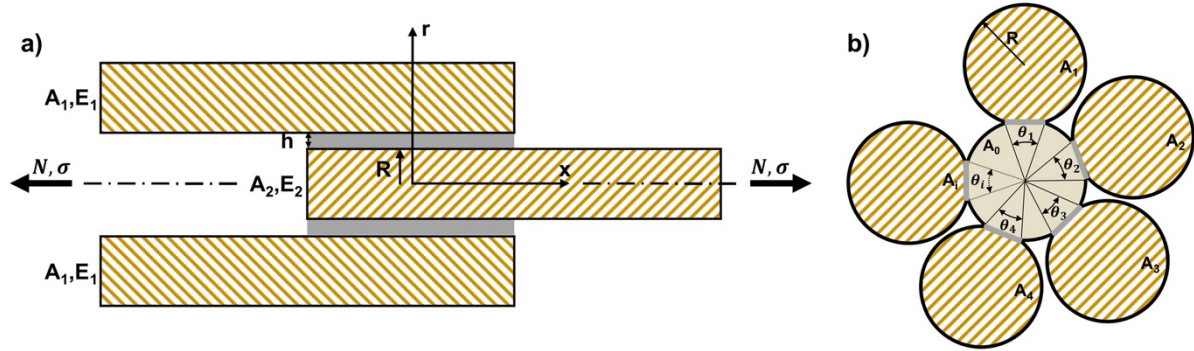
Figure S3. a) Depiction of tubular adhesive joint subjected to axial load, simplified for a tube-cylinder circular and co-axial contact mediated by an adhesive film, in grey. b) Schematic representation of the cross-section of previous joint for the case of several identical aligned microfibrils with partial adhesive contact described by θi. Ai are the cross-sections of the CMFs surrounding the central one, they have an Elastic Modulus of Ei. This configuration is depicting D, D+GO and D+SiC sample.

D, D+GO and D+SiC have equivalent cellulose microstructures (Fig. 2a), thus the only structural differences can be found in the interface layer, where nanoparticles are located. The differences between the concentric tubular configuration presented in [9] and our systems lies in the area of contact between different CMFs that is partial but have multiple areas of contact and does not extend to the entire external surface as for the tubes (Fig. S3a,b).

We propose to estimate if the nanoparticles at the CMF interfaces generate an increase in critical strain energy release at the microscale, which could cause the macroscopic enhancements in the stress of failure and toughness modulus in the D+GO and D+SiC samples (Fig. 3). Passing from a discrete analytical to a local model requires to substitute the axial force N with a constant distributed pressure σ on the x-axis that is generated as a consequence of the uniaxial tensile load conditions. The two models are linked if a catastrophic failure of the samples is considered. In particular, the bulk material exhibits a stable crack propagation when the applied load σ reaches a critical load σ_c, which is computed as the tensile strength of the mechanical tests.

Taking into account these considerations, Eq.1 can be rewritten to better suit the configuration of CMF in cellulose nanocomposites. The partial contact between CMFs is depicted in Fig. S3b where the central fibril is in contact with multiple fibrils, each for an arc of $\theta_i R$. As the nanoparticles are filling vacancies inside the structure, the key in comparing different samples is that the contact area between microfibrils remains unchanged in D, D+GO, D+SiC, hence nanoparticles play a role only in the determination of fracture energy Ga. Comparing the results with the analytical case in [9], we can consider crack nucleation to be a statistical phenomenon since the problem is symmetrical. This scrutiny implies that two terms in the ratio between axial rigidities in Eq.1 can indifferently be inverted and thus the ratio can be considered equal to 1 for cellulose nanocomposites. Finally, the following correlation is obtained:

$$\sigma_c \propto \sqrt{\sum_i (\theta_i R) \cdot G_a \cdot \left[E_0 A_0 + \sum_i (E_i A_i) \right]} \quad (2)$$

Eq. 2 links the failure strength to the critical value of strain energy release rate (G_a), i.e. fracture energy of the interface, for which the crack propagates [8, 9]. E_i and E_0 are to be considered identical since the load bearing structure of the composite is the same, so they can be reduced to E and extracted from the summation. To compare different sample groups (D, D+GO, D+Si), a second index j is inserted to label the quantities dependent on the three groups.

$$\sigma_{c,j} \propto \sqrt{\sum_i (\theta_{i,j} R_j)} \cdot \sqrt{\sum_i A_{i,j}} \cdot \sqrt{E_j G_{a,j}} \quad (3)$$

The first two terms in the product in Eq.3 are identical under the hypothesis of identical configuration and microstructure, therefore the relation can be rewritten as follows:

$$\sigma_{c,j} \propto \sqrt{E_j G_{a,j}} \quad (4)$$

where the tensile strength σ_c is a function of E_j, $G_{a,j}$, which are sample-related values. E_j was computed as the elastic modulus measured upon tensile testing for each sample. Then, the average improvements in interfacial fracture energy for the two set of nanoparticles can be computed:

$$\frac{\bar{G}_{a,D+GO}}{\bar{G}_{a,D}} = \frac{\bar{\sigma}^2_{c,D+GO}}{\sigma^2_{c,D}} \cdot \frac{\bar{E}_D}{\bar{E}_{D+GO}} \quad (5a)$$

$$\frac{\bar{G}_{a,D+SiC}}{\bar{G}_{a,D}} = \frac{\bar{\sigma}^2_{c,D+SiC}}{\bar{\sigma}^2_{c,D}} \cdot \frac{\bar{E}_D}{\bar{E}_{D+SiC}} \quad (5b)$$

where the two ratios $G_{a,D+GO}/G_{a,D}$ and $G_{a,D+SiC}/G_{a,D}$ represent the average interfacial fracture energy improvements for the 2 sets of nanocomposite reed. They are linked with the average failure stress $\sigma_{c,j}$ and elastic modulus E_j of each set of samples. The results show that the intercalation of GO the interfacial fracture energy is improved by 28%, and by 47% after SiC intercalation.

Interfacial fracture energy improvements	
$\dfrac{\bar{G}_{a,D+GO}}{\bar{G}_{a,D}}$	**1.28±0.33**
$\dfrac{\bar{G}_{a,D+SiC}}{\bar{G}_{a,D}}$	**1.47±0.36**

Table S1. Interfacial fracture energy improvements for D+GO and D+SiC samples.

In summary, the estimation of the interfacial fracture energy improvements in Table S1 are in line with the results of the mechanical tests that show a higher tensile and flexural performance after the intercalation of SiC nanoparticles rather than GO. Finally, a linear correlation is obtained between elastic strain energy release rate and toughness modulus reported in Fig. 3f.

Note 4 - Video of the burning tests

Attached file: Video S1 - Burning tests.

List of Abbreviations

GO graphene oxide; SiC silicon carbide; R giant reed; TC thermo-compressed; D densified; D+GO densified + graphene oxide; D+SiC densified + silicon carbide; CMF cellulose microfibril; XPS X-ray photoelectron spectroscopy; DSC differential scanning calorimetry; TGA thermogravimetric analysis; EDX energy dispersive X-ray; SEM scanning electron microscope

References

1. Gargulak, J. D.; Lebo, S. E.; McNally, T. J., Lignin. *Kirk-Othmer encyclopedia of chemical technology* **2001**.
2. Beamson, G.; Briggs, D., High resolution XPS of organic polymers: The Scienta ESCA 300 database. *Surface and Interface Analysis* **1992**, *20* (3), 267-267.
3. Goda, K.; Sreekala, M.; Gomes, A.; Kaji, T.; Ohgi, J., Improvement of plant based natural fibers for toughening green composites—Effect of load application during mercerization of ramie fibers. *Composites Part A: Applied science and manufacturing* **2006**, *37* (12), 2213-2220.
4. Li, X.; Tabil, L. G.; Panigrahi, S., Chemical treatments of natural fiber for use in natural fiber-reinforced composites: a review. *Journal of Polymers and the Environment* **2007**, *15* (1), 25-33.

135   5.   Li, Y.; Ruan, R.; Chen, P. L.; Liu, Z.; Pan, X.; Lin, X.; Liu, Y.; Mok, C.; Yang, T., Enzymatic hydrolysis of corn
136   stover pretreated by combined dilute alkaline treatment and homogenization. *Transactions of the ASAE*
137   **2004,** *47* (3), 821.
138   6.   Fratzl, P.; Burgert, I.; Gupta, H. S., On the role of interface polymers for the mechanics of natural polymeric
139   composites. *Physical Chemistry Chemical Physics* **2004,** *6* (24), 5575-5579.
140   7.   Gent, A.; Yeoh, O., Failure loads for model adhesive joints subjected to tension, compression or torsion.
141   *Journal of Materials Science* **1982,** *17* (6), 1713-1722.
142   8.   Pugno, N.; Carpinteri, A., Strength, stability and size effects in the brittle behaviour of bonded joints under
143   torsion: theory and experimental assessment. *Fatigue & Fracture of Engineering Materials & Structures* **2002,**
144   *25* (1), 55-62.
145   9.   Pugno, N.; Carpinteri, A., Tubular adhesive joints under axial load. *Journal of applied mechanics* **2003,** *70* (6),
146   832-839.

147